CHAPTER 2

Literature Review

Contents:

2.1. Introduction:

The literature survey was conducted to fulfill the research motivation and objectives of the reported work. The review provides valuable insights into the research gaps, fundamental properties, and recent advances relevant to the objectives of this thesis. It is essential for establishing a foundational understanding of the field and enabling informed decision-making in the development of 2D-WS_2-based FET.

This study mainly focuses on the application of WS_2 in FET devices, in which the preparation of WS_2 materials is an important aspect of research. The study also explores methods to enhance its electronic properties for improved device performance. Furthermore, the fabrication processes of WS_2-based FETs were examined, highlighting their advantages and addressing the associated challenges. Through this comprehensive review, the objective is to acquire essential knowledge to guide experimental strategies, fabrication processes, and achieve performance metrics that meet the demands of advanced 2D electronics.

Additionally, the survey delves into the intrinsic properties and behaviour of 2D-WS_2 nanosheets, which are pivotal for their application in FET devices. By exploring characteristics such as electronic band structure, charge carrier mobility, and band gaps, this review aims to identify key parameters that significantly influence the performance of WS_2-based devices. This literature survey forms the basis for the subsequent experimental work, ensuring that the research objectives are addressed effectively.

2.2. Properties of 2D-WS_2:

WS_2 has garnered significant attention due to its ultrathin atomic layer structure and semiconducting properties, which can be tailored for specific applications. Each layer of WS_2 consists of a plane of W atoms sandwiched between two layers of Sulfur (S) atoms, with the atoms covalently bonded to the adjacent atoms. While the layers of WS_2 are bonded together by weak vdW forces, enabling easy separation through exfoliation techniques. Furthermore, WS_2 has a relatively high bandgap that changes with the number of layers, the change in bandgap is directly linked to the physical and electrical properties of the material [1–4]. WS_2 is commercially available in various forms, such as bulk powder or crystal, which can be exfoliated into thin nanosheets. Additionally, WS_2 can be synthesized into nanosheets with adjustable size and thickness, depending on the preparation process such as vapor phase deposition, chemical synthesis method, etc.

WS_2 is known for its n-type semiconducting behaviour, and the indirect bandgap of its multilayer structure makes it well-suited for efficient FET operation [5,6]. Theoretical studies suggest that WS_2 has superior electrical properties, featuring high carrier mobility, an excellent bandgap, and outstanding chemical stability compared to other 2D TMDs [7–9]. Furthermore, WS_2 exhibits excellent temperature tolerance and inherent flexibility, making it ideal for various wearable applications [10,11]. These attributes allow WS_2-based devices to perform reliably under diverse environmental conditions, meeting the demands of advanced flexible electronics. Researchers have emphasized the need for precise control over the film structure of WS_2 to optimize its performance, with monolayer and multilayer films being suitable for optoelectronic applications and electronics applications [12,13].

Theoretical models for WS_2 FETs have shown that their on-current is 1.5 times higher than other 2D-FET transistors, with high mobility due to the reduced effective mass of carriers [14]. Jin et al. reported that the intrinsic electrical properties of single-layer WS_2 FETs are comparable for both n-type and p-type FETs, highlighting its potential as a versatile candidate for transistor channel applications [15]. However, experimental electron mobility values for single-layer WS_2 FETs are currently lower than theoretical predictions, with values of ~50 $cm^2/V{\cdot}s$ at room temperature. Studies have shown that multilayer WS_2 FETs exhibit promising performance at low temperatures ~5 k, with reduced Schottky barriers at the Metal-WS_2 interface, and observed mobility values of ~234 $cm^2/V{\cdot}s$ at room temperature [16]. WS_2 is notable for its strong spin-orbit coupling, which causes significant valence band splitting and spin-valley coupling. These effects are amplified by the heavier tungsten atoms, making WS_2 more pronounced in these properties compared to MoS_2 [17]. This results in a valence band splitting of approximately 426 meV, which is three times larger than MoS_2, facilitating the observation of the valley Hall effect [7]. Additionally, WS_2 has Young's modulus (~150 GPa) makes it mechanically robust at the nanoscale and suitable for integration into flexible and wearable electronics. WS_2 TFTs have shown the ability to withstand up to 50,000 bending cycles with minimal degradation, demonstrating their potential for flexible and durable devices [18]. These combined properties position WS_2 as a promising material for next-generation high-performance electronic applications.

2.2.1. Structural Analogy of 2D-WS_2 Materials:

The WS_2 crystals consist of strong in-plane covalent bonds between W atoms, with each W atom positioned between two S atoms in a hexagonal lattice arrangement. This configuration forms a two-dimensional structure, where robust covalent bonds between W and S atoms contribute to a highly stable and strong layer. WS_2 exists in three distinct crystal phases: the 1T phase exhibits metallic behaviour, while the 2H and 3R phases are semiconducting.

- **1T-Phase:**

The 1T phase of WS_2 is depicted in Fig. 2.1(a), exhibits a structure of tetragonal symmetry (space group P21/m) with Octahedral (Oh) coordination, belonging to the D_{3d} point group. This phase is characterized by two sets of degenerate d orbitals: dz^2,x^2-y^2 (eg) and dxy,yz,zx (t_{2g}) [19, 20]. The presence of one electron in each t_{2g} orbital results in partially filled orbitals, which contribute to the metallic nature of the 1T phase [21]. The atomic stacking sequence in the 1T phase follows an A-B-C pattern, with W atoms positioned at the center of the octahedral coordination. In 1972, R. B. Somoano et al. introduced an alkali metal intercalation method that enabled the transformation of 2H-phase TMDs into the 1T phase, emphasizing the role of lithium and sodium as intercalating agents. This process involves the incorporation of additional charges from lithium, which induces a local atomic rearrangement that alters the structure from trigonal prismatic (2H) to octahedral (1T). Despite being less stable and commonly synthesized in monolayer form, the 1T phase possesses exceptional properties, including high efficiency as an electrocatalyst and excellent electronic conductivity. However, due to its metallic nature, the 1T phase lacks significant optical absorption and emission capabilities. Although less stable and typically synthesized in monolayer form, it exhibits unique properties, serving as a highly efficient electrocatalyst and an excellent electronic conductor [22, 23].

- **2H-Phase:**

Fig. 2.1(b). represents the 2H phase of WS_2 belonging to the space group $P6_3/mmc$ D_{6h} (no. 194) and adopts a trigonal prismatic configuration (D_{3h}). In this configuration, the d-orbitals are split into three groups: a single filled dz^2 orbital and two empty sets of double-degenerate orbitals dx^2-y^2,xy and dxz,yz [20]. The 2H-WS_2 phase exhibits semiconducting behaviour due to its fully occupied dz^2 orbital. Structurally, the 2H phase

features an A-B-A stacking sequence, with W atoms occupying the center of the triangular prisms [24]. This phase consists of two layers per unit cell along the c-axis, forming a hexagonal symmetrical structure. The distance between two W atoms in the same plane within the hexagonal lattice is represented by lattice constants of approximately 3.15 Å (in-plane) and vertical spacing between two adjacent layers of WS_2 is 6.15 Å (interlayer distance). This layered arrangement not only enables anisotropic properties but also underlies the transition from an indirect bandgap (~1.4 eV in bulk) to a direct bandgap (~2.1 eV in monolayer form)[16,25]. This transition is attributed to quantum confinement, which modifies the hybridization between the S and W orbitals, thereby altering the electronic band structure [26]. Furthermore, the band structure of the 2H phase can be tuned through doping, which introduces changes to the atomic lattice of WS_2 [27]. The 2H phase is thermodynamically stable, occurring naturally (Blue-gray colour in its powdered or crystal form) and maintaining its stability under ambient conditions. To achieve thin or monolayer WS_2 structures for device applications, the material is typically exfoliated from bulk crystals or synthesized at high temperatures [28,29]. The layers of WS_2 are held together by weak electrostatic forces, which enable easy exfoliation into monolayers or few-layer structures from the bulk crystal or powder. In the 2H-phase structure, the high indirect bandgap imparts superior semiconducting properties, making it suitable for transistor applications. Additionally, it has poor electrocatalyst, high optical absorption, strong photoluminescence, and significant light-harvesting potential, making it valuable for optoelectronic applications in its monolayer form [30,31].

- **3R Phase:**

The 3R phase of WS_2 as shown in Fig. 2.1(c), where "R" denoting its rhombohedral symmetrical structure (C_{3v}^5 group) belongs to the space group R3m, No 160 is a rare structural form that does not occur naturally [25, 32]. The 3R phase of WS_2, being a rare structural form, necessitates synthetic production through controlled methods such as molecular beam epitaxy, chemical vapor deposition or other specialized techniques is used to grow rhombohedral symmetry and unique stacking arrangement [33]. Like the 2H phase, the 3R structure exhibits semiconducting properties but plays a less prominent role in semiconductor applications due to less consistency in bandgap tunability, less stability, and prone to transformation into the 2H phase under certain conditions [25]. It features a three-layer stacking sequence per unit cell, similar to the 2H phase, but with distinct structural periodicity [34]. The 3R structure exhibits semiconducting properties;

however, its application in semiconductor technologies is limited due to less consistent bandgap tunability, lower stability, and a tendency to transform into the thermodynamically stable 2H phase under certain conditions. Unlike the 2H phase, which offers tunable, layer-dependent bandgap properties and is naturally abundant, the 3R phase lacks such flexibility, reducing its suitability for precision applications [32].

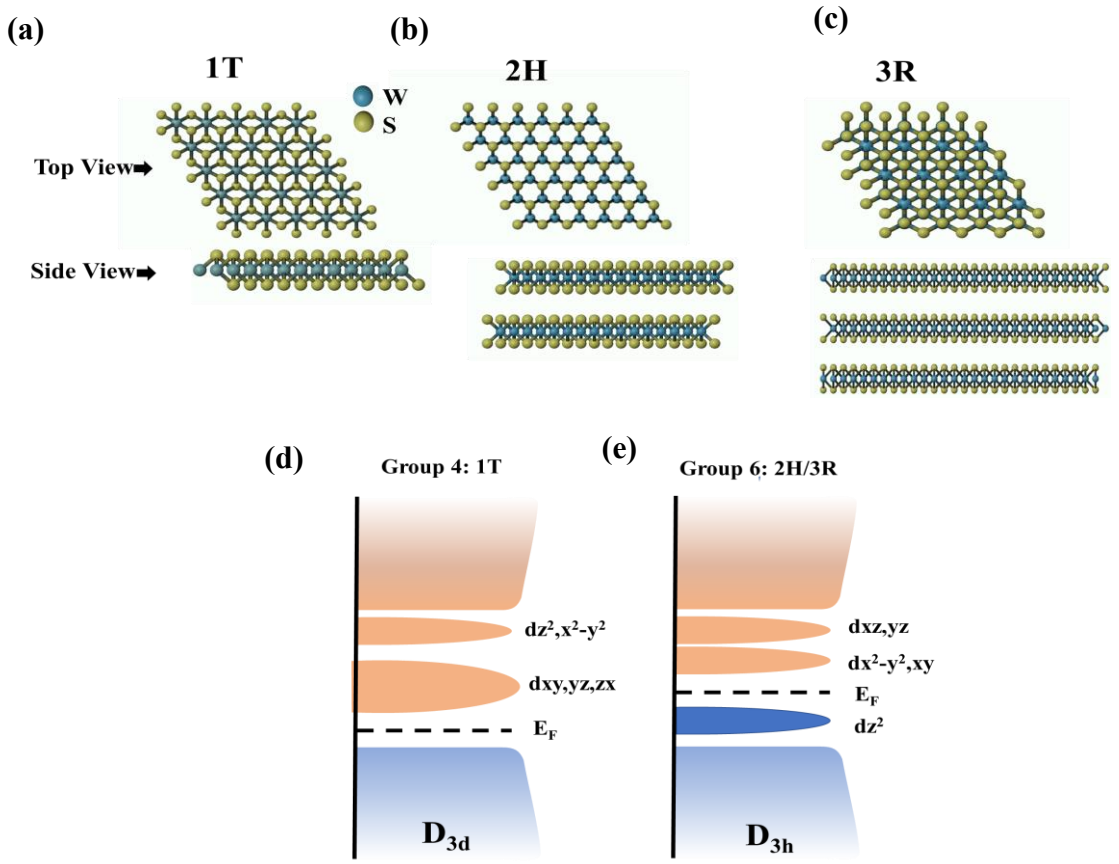

Fig. 2.1: Atomic structure of three typical crystal phases of WS_2: (a)1T-phase tetragonal symmetry with octahedral coordination (b) 2H-Phase hexagonal symmetrical structure (c) 3R-Phase rhombohedral symmetrical structure and (d & e) schematic illustration of the density of states for selected transition metal groups, showing the d-orbital splitting for 1T and 2H/3R phase

According to the reported data, the 2H phase of WS_2 is regarded as the best option for transistor applications, outperforming the 1T and 3R phases due to several key factors. The 2H phase is naturally abundant and stable under ambient conditions, which makes it ideal for practical device fabrication. Unlike the 1T phase, which exhibits metallic behaviour and lacks the semiconducting properties necessary for transistor operation, the 2H phase is a stable semiconductor with well-defined electronic properties. In contrast,

the 3R phase, while semiconducting, is less stable and prone to transformation into the 2H phase under certain conditions, making it less reliable for consistent transistor behaviour. The studies focused on investigating 2H-WS_2 for its potential in semiconductor applications. The physical properties of WS_2 are detailed in Table 2.1.

Table 2.1: Structural properties of WS_2

WS_2			Ref. No.
Lattice Constant (Å)	a:	3.15	[35]
	c:	12.32	
Vander Wall Gap (Å)	S-S	3.15	
Interlayer Height (Å)	S– W	3.41	
Bond Angle (degree)	S–W–S	80.99	
Interlayer Spacing (Å)	d-spacing	6.15	[36]

2.2.2. Energy Band Structure and Bandgap Tuning of WS_2:

2D TMDs are indeed considered promising materials for semiconducting applications owing to their adjustable bandgap, which provides an advantage over zero-bandgap graphene in many electronic and optoelectronic applications [37,38]. The bandgap plays a critical role in practical applications, as changes in the bandgap significantly influence the material's properties.

This section focuses on the study of the bandgap properties of WS_2 material belonging to the class of TMDs. Theoretically, Density Functional Theory (DFT) is employed to determine the bandgap of WS_2, while UV-Vis and PL spectroscopy are utilized for bandgap analysis in practical applications [39]. Fig. 2.2 illustrates the DFT-calculated indirect and direct band structures of WS_2, indicating that the bandgap of WS_2 material is dependent on the layers present in nanosheet [40]. These can significantly affect the optical and electrical properties of the material. As the number of layers in WS_2 decreases, the material undergoes significant transformations in its energy band structure, particularly as it transitions from multilayer to monolayer form. In multilayer WS_2, the material exhibits an indirect bandgap, with the Conduction Band Minimum (CBM) at an intermediate point (Λ) and the Valence Band Maximum (VBM) at the Γ point in the Brillouin zone as depicted in Fig. 2.2(a) [3,41]. In contrast, multilayer WS_2 nanosheets exhibit an indirect bandgap, making them suitable for electronic devices. These multilayer structures offer superior electron transition properties and high carrier mobility, thereby enhancing the electrical properties of WS_2-based semiconductors [16].

However, when the multilayer is reduced to a monolayer, WS_2 shifts to a direct bandgap with both the CBM and VBM located at the K point as depicted in Fig. 2.2(b) [2,38,42]. The reduction in layer number causes the WS_2 bandgap to shift from the infrared region to the visible region and it also changes the bandgap from indirect to direct. This direct bandgap enables more efficient photon absorption and emission, enhancing the potential for optoelectronic applications [43]. Additionally, as layer thickness decreases, the bandgap energy widens due to weakened interlayer coupling, which reduces electronic overlap between layers. Spin-Orbit Coupling (SOC) further influences the band structure, causing distinct splitting in the valence band at the K point, a feature that becomes more prominent in the monolayer and impacts optical transitions. The weakening of interlayer coupling also affects van der Waals interactions, which contributes to these changes in the bandgap and electronic structure, making monolayer WS_2 material. The bandgap comparison of Si and 2D semiconductor materials is demonstrated in Table 2.2.

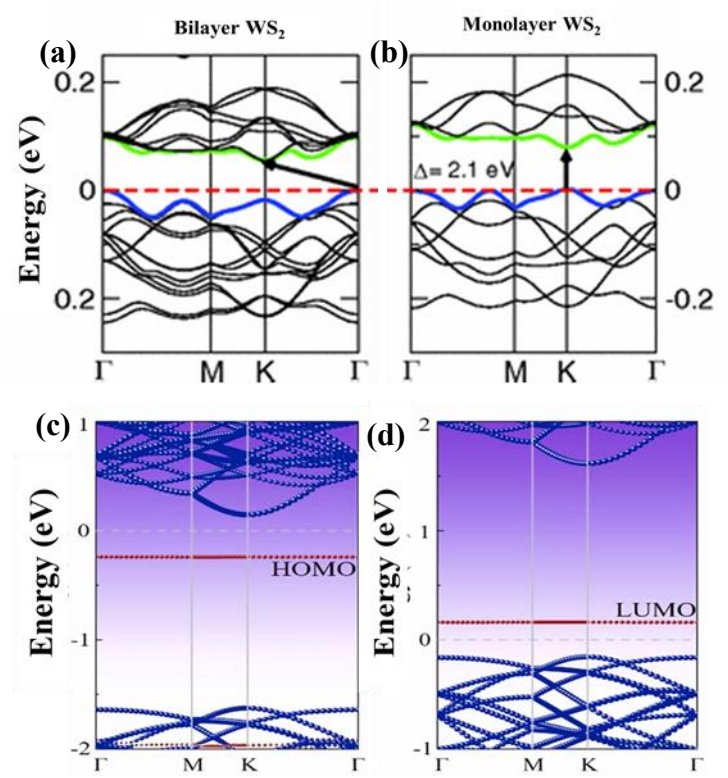

Fig. 2.2: Band structure of 2H-WS_2: (a) Indirect bandgap of bilayer WS_2 (b) Direct bandgap of monolayer WS_2 [40], (c) band structure of p-type doped WS_2 and (d) Band structure of n-type doped WS_2 [44]

In addition, the variations in the band structure of WS_2 are primarily driven by quantum confinement effects that arise from doping and edge effects [45]. Studies have shown that the bandgap, as well as the shifts in the valence and conduction bands, can be tuned through doping or the introduction of vacancies in the atomic lattice of WS_2. These doping strategies not only alter the bandgap but also modify the material's electronic properties. WS_2 generally exhibits n-type semiconducting behaviour, which can be adjusted depending on the type of dopant atom used [46, 47]. Yang et al. demonstrated that molecular doping with n-type or p-type dopant atoms can modify the band structure of WS_2 [44]. In the case of n-type doping, a deep impurity level appears below the conduction band minimum after the WS_2 adsorbs a Tetrathiafulvalene (TTF) molecule. This impurity level is primarily derived from the Highest Occupied Molecular Orbital (HOMO) as depicted in Fig. 2.2(c). For p-type doping using Tetracyanoquinodimethane (TCNQ), the injection of holes into the material, associated with the Lowest Unoccupied Molecular Orbital (LUMO), causes the valence band to shift closer to the Fermi level as demonstrated in Fig. 2.2(d). Chanana et al. reported that the bandgap of WS_2 can be modified through n-type doping [48]. In their study, the bandgap of a pure monolayer of WS_2 was found to be 2.07 eV. When a single chlorine atom is used as a dopant, the energy bands shift toward the Fermi Level (E_F), creating midgap states near E_F and leading to an increase the bandgap 2.12 eV. This shift is attributed to the hybridization of the Cl 3p and W 5d states, with an additional unpaired electron introduced due to the n-type doping by chlorine. The CH groups acted as p-type dopants, proving to be the most stable method for introducing carbon into WS_2 [49]. This led to a reduction in the bandgap from 1.98 eV to 1.83 eV, as measured by PL spectroscopy. The energy level of the top valence band was primarily influenced by the d orbitals of W and the p orbitals of Carbon (C), suggesting that the formation of a W-C bond is the main factor responsible for the observed bandgap reduction.

Table 2.2: Bandgap comparison of Si and 2D semiconductor materials

Material	Bandgap (E_g) (eV)	Layer number	Applications	Ref. No.
WS_2	1.94	Single layer	-	[41]
	1.588	Bilayer		
	0.88	bulk		
Si	1.1	-	Semiconductor	[50]
Graphene	0	-	Semiconductor	[51]
WS_2	2.11	Monolayer	Optical	[52]

WS_2	1.883	Multilayer	electrical	[53]
WS_2	~1.25	Six-layer	-	[54]
	~1.45	Four-layer		
	~1.8	Monolayer		
MoS_2	1.8	Monolayer	-	[55]
	1.2	Bulk		
MoS_2	1.89	Monolayer	-	[56]
MoS_2	1.9	Monolayer	FET	[57]
	1.2	Four-layer		
WSe_2	1.6	Monolayer	-	[58]
	1.4	Few-layer		
$MoSe_2$	1.48	Monolayer	-	[59]
	1.10	Bulk		
$MoTe_2$	1.1	Monolayer	Optoelectronics	[60]
$MoTe_2$	1.04	Monolayer	Optoelectronics	[61]

2.2.3. Synthesis Processes of Layered 2H-WS_2 Material:

A wide range of approaches for synthesizing layered WS_2 material have been reported by various authors. These methods are generally categorized into two types: top-down and bottom-up approaches [12,62,63]. Top-down approaches involve exfoliation techniques, where nanosheet layers are peeled from bulk material, such as mechanical exfoliation, liquid exfoliation, etc. In contrast, bottom-up approaches include vapor-phase deposition, atomic layer deposition, hydrothermal methods, etc., where the material is built up from individual atoms or molecules [12, 64].

2.2.3.1. Top-down Synthesis:

- **Mechanical Exfoliation:**

In 2004, Novoselov et al. first demonstrated the synthesis of graphene using a mechanical exfoliation process, a simple and highly efficient technique for producing monolayer or few-layer 2D materials [62]. It involves the use of adhesive tape to peel thin layers from bulk materials by exploiting weak interlayer bonds, enabling the production of single or multi-layer flakes without the need for external heating [65]. The exfoliation process is visually represented in Fig. 2.3(a). Following the discovery of graphene, micromechanical exfoliation has been successfully used to exfoliate other 2D layered materials, including the TMD, BP, h-BN, etc. In semiconductor device fabrication, Radisavljevic et al. first demonstrated the fabrication of a FET using a monolayer MoS_2 flake extracted from a commercially available MoS_2 single crystal [66]. It has also been particularly useful in successfully producing atomically thin WS_2, enabling researchers

to explore its unique properties and potential applications [67]. While mechanical exfoliation is effective for producing 2D materials, its limited scalability restricts its feasibility for mass production. For large-scale fabrication of 2D devices, more scalable techniques are essential. However, mechanical exfoliation is a low-cost method that is highly convenient for fundamental research.

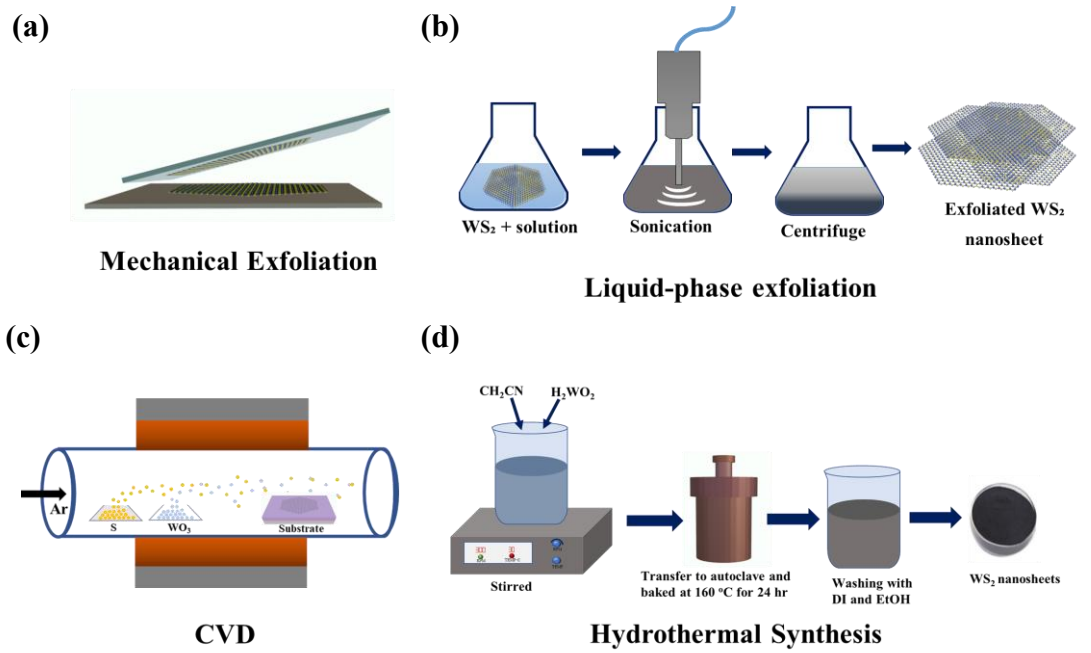

Fig. 2.3: Schematical illustration of commonly adopted synthesis method for producing 2D materials: (a) Mechanical exfoliation using scotch tape to extract layers from bulk WS_2 (b) Liquid-phase exfoliation, producing layered nanosheets from bulk WS_2 powder through sonication in a suitable solvent (c) Experimental setup illustrating the Vapour phase deposition technique: thermal evaporation of WO_3 powder and chalcogen (S) powder to produce layered 2H-WS_2 and (d) Hydrothermal method for synthesizing WS_2 in an autoclave at high temperature and pressure

- **Liquid-Phase Exfoliation:**

LPE is an extensively studied method for producing 2D-materials from bulk-layered materials. This technique has been explored since the early 1970s and offers a relatively simple, room-temperature approach to obtain thin, exfoliated layers [63]. In LPE, suitable solvents need to be mixed with bulk material, which is then subjected to sonication to weaken the interlayer bonds between the layers [68]. The sonication process creates vibrations that break the vdW forces holding the layers together, allowing them to separate. Coleman et al. demonstrated that layered materials can be effectively

exfoliated using a range of organic solvents and surfactants in aqueous solutions, with the exfoliated material typically separated through centrifugation [64]. D'Olimpio et al. reported that Iris-assisted LPE process enables the production of exfoliated flakes with a high yield of up to 52%. Additionally, this technique achieves flakes with an exceptionally high aspect ratio, reaching values as high as 500 [69]. Commonly used solvents for exfoliating 2D materials include high-boiling-point solvents such as N-Methyl-2-Pyrrolidone (NMP) and N-Dimethylformamide (DMF) [70]. Additionally, liquid exfoliation using a binary mixture of Acetone (ACE) and water has been shown to yield approximately 2.7%, which is considered promising for the large-scale production of nanosheets [71]. Despite certain challenges, such as limited stability, LPE remains a promising method for the scalable production of 2D materials. It enables the fabrication of high-quality, large-area thin films consisting of only a few layers.

2.2.3.2. Bottom-up Synthesis:

- **Vapour Phase Deposition:**

Vapor phase synthesis is classified into two main types: physical vapor deposition (PVD) and CVD. In PVD, commonly used methods include thermal evaporation, Molecular Beam Epitaxy (MBE), and van der Waals epitaxy (VDWE). These methods rely on physical processes, such as heating and evaporation, to deposit thin films on a substrate. While PVD is effective for controlled deposition, some PVD techniques such as Pulsed Laser Deposition (PLD) and Electron Beam Evaporation (EBE)-often result in unwanted morphologies like nanoparticles instead of the desired layered structure. In addition, those techniques have low deposition rates, very low vacuum, and are generally very expensive. This can limit their suitability for producing 2D layered nanosheets.

CVD is one of the most widely used techniques for producing large-area, atomically thin WS_2 nanosheets. CVD allows precise control over nanosheet thickness, making it highly effective for synthesizing layered 2D materials. In the CVD process, a tungsten precursor (like WO_3 powder) and S powder are vaporized and react at specific temperatures in a controlled environment. An inert carrier gas, such as argon or nitrogen, flows continuously to transport these vapours to the substrate, where WS_2 nanosheets grow directly [31]. The experimental setup for the CVD process used to grow 2D WS_2 nanosheets is schematically illustrated in Fig. 2.3(c). In this technique, WO_3 is first deposited onto a substrate in a nanometer-scale layer, followed by sulfurization at temperatures above 500 °C [12]. This results in the direct formation of an atomically thin

WS_2 layer on the substrate, offering an effective pathway for producing uniform, high-quality WS_2 nanosheets. An et al. reported that CVD-grown WS_2 monolayer flakes via Oxygen (O_2) pre-annealing process to obtain of triangular and hexagonal shapes of nanosheets is dependent on the O_2 flow rate [72]. Twisted Bilayer WS_2 (TB-WS_2) is directly grown on a SiO_2/Si substrate inside a quartz tube, with the substrate placed at an angle. This tilting creates an uneven concentration of the metal precursor, causing disturbances in the gas flow over the substrate. These disturbances provide an additional driving force that promotes the growth of TB-WS_2 is reported by Xu et al. [73]. Yan et al. demonstrated the synthesis of high-quality WS_2 nanosheets with diverse morphologies, including large triangular, hexagonal, small triangular, terraced, and spiral structures [74]. These nanosheets were produced through the CVD process at a growth temperature of 850 °C, with an Argon (Ar) gas flow rate controlled in standard cubic centimeters per minute (sccm).

- **Hydrothermal Synthesis:**

One of the simple and facile techniques for synthesizing WS_2 is the hydrothermal method, which is a conventional wet chemical synthesis approach as shown in Fig. 2.3(d). This method has been extensively employed for the synthesis of 2D nanomaterials. In this process, the atomic reaction is formed in a suitable solvent at a certain temperature [75]. Santhosh et al. reported the preparation of WS_2 nanosheets using a two-step hydrothermal method, conducted at 245 °C for 8 hours [76]. Govindasamy et al. synthesized MoS_2 and WS_2 nanoparticles using an ultrasonic-assisted hydrothermal method, where Mo or W powder was mixed with Thioacetamide in DI water were sonicated, then heated at 180 °C for 2 hours in an autoclave [77]. The resulting precipitate was washed with Deionized water (DI) and Ethanol (EtOH) and then dried to obtain WS_2 powder. Within the hydrothermal process, high temperature and pressure accelerate the chemical reactions, promoting the formation of WS_2 nanoparticles. Hydrothermal synthesis is a relatively simple and low-cost technique but typically results in lower-quality WS_2 compared to vapor-phase growth techniques [78]. Furthermore, the thickness of the films cannot be accurately controlled for device applications, and the reaction process cannot be directly monitored.

2.2.4. Techniques of 2D Material Transfer Methods for Electronic Devices Fabrication:

One of the critical steps in the fabrication of TMD-FET is the transfer of WS_2 nanosheets onto the designated substrate, which can be accomplished through either a dry transfer or wet transfer process. The physical and crystalline properties of the 2D materials remain largely unaffected by these transfer techniques. Both transfer processes are straightforward and cost-effective.

2.2.4.1. Wet Transfer:

- **Chemical Etching Wet Transfer:**

Fig. 2.4(a) illustrates the chemical etching transfer process, where the grown 2D material is initially coated with a Poly (Methyl Methacrylate) (PMMA) layer via the spin-coating technique. [79,80]. The substrate is then etched by placing it in a chemical etchant (potassium hydroxide or ammonium persulfate for copper). After etching, the WS_2/PMMA layer floats on water and can be easily transferred to the desired substrate. Finally, the PMMA is dissolved in acetone by dipping the WS_2-transferred substrate, leaving a clean WS_2 film on the new substrate [81].

- **Electrochemical Bubble Transfer:**

Another wet transfer technique is the etchant-free electrochemical bubbling method, which is a non-destructive, cost-effective, and time-efficient process illustrated in Fig. 2.4(b) [82]. In this method, the PMMA-2D material-coated substrate is immersed in a suitable electrolyte solution (e.g., $K_2S_2O_8$, NaOH or Na_2SO_4). An electrode is then connected to the substrate, with both submerged in the same solution, to establish a potential difference between the substrate and the electrode [83]. As a direct consequence of this polarization, hydrogen bubbles emerge at the interface of PMMA-2D material with the substrate and bubbles move inward until the material is completely detached from the substrate. Then the same chemical etching Wet transfer process is followed for transferring the 2D material on the targeted substrate for device fabrication [83,84].

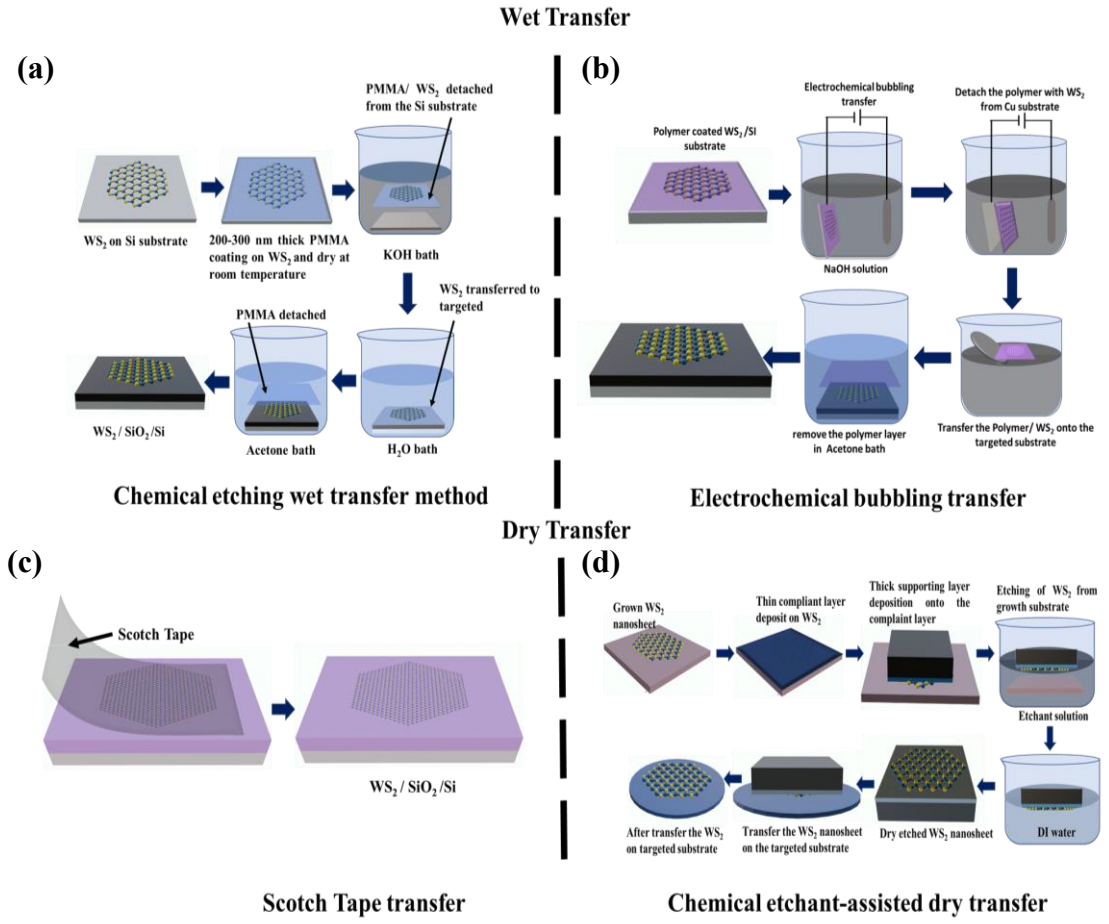

Fig. 2.4: Illustrative depiction of 2D material transfer methods by dry and wet transfer techniques: (a) Chemical etching wet transfer (b) Electrochemical bubble transfer (c) Scotch tape dry transfer and (d) Chemical etchant-assisted dry transfer method

2.2.4.2. Dry Transfer:

The dry transfer of 2D materials is a simple, inexpensive, yet time-consuming method. The process involves either mechanical transfer using scotch tape or a chemical etchant-assisted dry transfer technique.

- **Scotch Tape Transfer:**

In mechanical transfer, scotch tape is used to peel off the 2D material from the grown substrate, and the 2D material is then directly transferred to the designated substrate as shown in Fig. 2.4(c) [85,86]. This method does not require any chemicals or solvents.

- **Chemical Etchant-Assisted Dry Transfer:**

For the chemical etchant-assisted dry transfer method, it is more suitable for large-scale applications [85]. Initially, a polymer, usually Polydimethylsiloxane (PDMS),

combined with a supporting layer of Poly(Ethylene Terephthalate) (PET) substrate, is deposited onto the 2D material as represented in Fig. 2.4(d) [87]. The 2D material is then detached from the grown substrate like wet transfer. Once the material is on the PDMS/PET substrate, it must be dried before being transferred to the targeted wafer. The PDMS/PET substrate, now coated with the 2D material, acts as a stamp that is placed onto the targeted wafer. The PDMS/PET is then peeled off without the use of any solvents.

2.3. 2H-WS_2 in FET Application:

The WS_2-FET has emerged as an advanced electronic device in which 2H-WS_2 serves as the channel material. WS_2-FETs offer potential applications in diverse electronic devices, including sensors, photodetectors, and switching components. The electrostatic response of the WS_2-FET is influenced by the atomic layer thickness of the nanosheets. Various FET structures, including back-gated, top-gated, and dual-gated-FET, have been developed using WS_2 and other 2D materials [88,89]. The WS_2-FET exhibits excellent switching capability, enabling effective control of on/off-state performance at low voltage, which can be adjusted through the gate. The illustrative depiction of the WS_2-FET is represented in Fig. 2.5.

2.3.1. Back Gate FET Structure:

Back-gated FET devices are fabricated using SiO_2 or other dielectric layers as back-gate dielectrics [90]. These dielectric layers are deposited onto the substrate before placing the WS_2 semiconductor material to construct the FET. Typically, SiO_2-coated silicon substrates are utilized due to their commercial availability. Alternatively, high-k dielectrics like Hafnium Dioxide (HfO_2) [91], Aluminum Dioxide (Al_2O_3) [92], etc. can be deposited using Atomic Layer Deposition (ALD), providing enhanced electrostatic control for specific applications. The back-gated structure is particularly advantageous for studying TMD-based FETs as it provides consistent gate control, enabling efficient electrostatic manipulation. Chen et al. reported that Al_2O_3-based top-gated MoS_2 FETs exhibit a lower mobility of 0.31 $cm^2/V{\cdot}s$ compared to 1.71 $cm^2/V{\cdot}s$ in SiO_2-based back-gated FETs [93]. The reduced mobility is due to interface traps and defects introduced during Al_2O_3 deposition, which can degrade MoS_2 layers by forming Mo-oxide and increasing Coulomb scattering, thereby limiting carrier mobility. However, SiO_2 substrates exhibit a comparatively lower current on/off ratio than Al_2O_3.

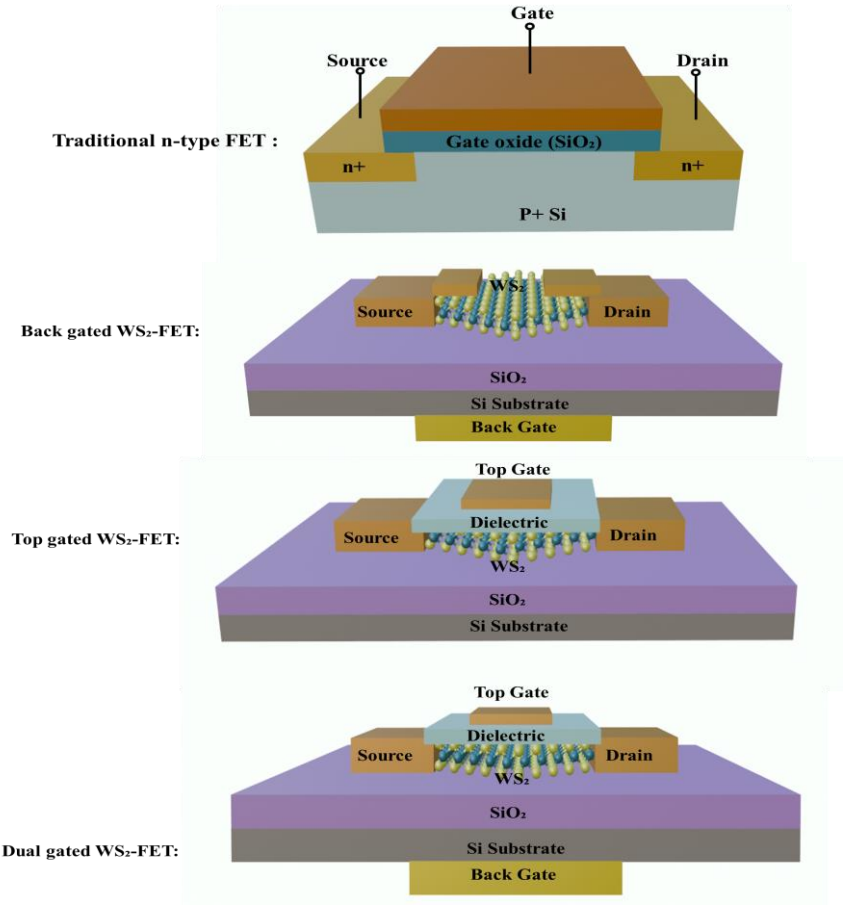

Fig. 2.5: Illustrative depiction of the traditional Si-based MOSFET and back-gate, top-gate and dual-gated WS_2-FET structure

2.3.2. Top Gate FET Structure:

In the top-gated WS_2-FET structure, the oxide dielectric is deposited directly onto the WS_2 nanosheet surface [94]. Due to the excellent chemical and thermal stability of WS_2, various dielectric materials inorganic and organic can be deposited on the nanosheet surface using techniques like ALD, sputtering, spin coating, etc. [95]. The top-gated FET offers higher operating performance, greater electron transport, and enhanced field-effect mobility, making it more effective than the back-gated FET [94,96]. Additionally, high-k dielectrics, such as HfO_2 or Al_2O_3, can be incorporated onto the nanosheet surface, reducing interface traps between the semiconductor and dielectric [95]. However, the top-gated FET faces challenges, such as achieving nonuniform deposition of the dielectric thin film due to dangling bonds on the WS_2 surface, which complicates interface engineering [97]. Yang et al. and Kim et al. reported that low-temperature (<100 °C) ALD deposition of Al_2O_3 dielectric layers raises significant concerns due to high levels of impurities, such as Hydroxyl (OH) groups and carbon residues, within the dielectric film

[98,99]. Additionally, achieving a uniform thin film on the surface of TMD materials remains challenging, complicating its practical application in FET devices.

2.3.3. Dual Gate FET Structure:

The dual-gated FET is a complex device structure, requiring two gates: one on the nanosheet surface, which serves as the top gate, and another on the backside of the device, functioning as the back gate [100]. This design adds steps to the fabrication process and increases complexity in the WS_2-FET. In this structure, SiO_2 is used as the back-gate dielectric, while a different dielectric material is employed for the top gate [4,101]. During electrical measurements, both gates were utilized with distinct configurations: in the top-gate biasing mode, the bottom-gate voltage was held constant, and in the bottom-gate biasing mode, the top-gate voltage was kept constant. Jin et al. investigated a dual-gated WS_2-FET employing a stack of Al_2O_3/SiO_2 as the back gate and Al_2O_3 as the top gate dielectric [102]. The study revealed that in the back-gate biasing mode, stronger accumulation occurred in the contact region, resulting in a lower contact resistance of 1.5 ± 3.6 kΩ·μm. In contrast, under top-gate biasing, the contact region was not fully accumulated, leading to a significantly higher contact resistance of 25.9 ± 3.6 kΩ·μm. Additionally, the dual-gated structure achieved a channel carrier concentration of 6.9×10^{12} cm^{-2}, demonstrating its effectiveness in enhancing device performance. This highlights the significant modulation of contact region conductivity by the bottom gate biasing mode, directly impacting R_C. The dual-gate configuration enhances the modulation of the device's conductivity, allowing for more precise control over the electrical transport properties of the WS_2-FET. However, the dual-gated WS_2-FET faces several challenges, including charge trapping and mobility degradation. Jin et al. reported that its mobility was lower than that of a back-gated FET [103]. Furthermore, the dual-gated structure exhibited hysteresis in the I-V characteristics, which was attributed to a higher density of trap charges in the gate region. Applying dielectric layers on 2D materials presents considerable difficulties because there are no dangling bonds or anchor points, which are crucial for the initial bonding of ALD precursors. The insufficient surface reactivity complicates the formation of a continuous and conformal ALD layer on the surface of the 2D material [104,105]. These issues can result in inadequate dielectric coverage, impacting the electrostatic control and overall efficiency of the device. Insufficient dielectric layers can lead to heightened gate leakage, diminished mobility,

and lower device reliability, all of which can significantly affect the performance of 2D-material-based FETs.

Experimental research on back-gated WS_2-FETs and their electrical characterization has been thoroughly investigated in this thesis. This work focuses on back-gated FET devices, which can help to reduce fabrication complexities. These devices were fabricated using commercially available SiO_2 and the back side Si serves as the back-gate contact, which can reduce the fabrication costs and eliminate the need for advanced lithography and deposition techniques. Moreover, direct deposition of dielectrics on 2D materials can often introduce defects, charge traps, or stress, adversely affecting the electrical performance of the device. The comparison of top-gated, bottom-gated, and dual-gated TMD-FETs is shown in Table. 2.3.

Table 2.3: Summary of performances of different Top, bottom and dual-gated TMD-FETs

TMD	Dielectric	Gate type	μ_{FE} (cm^2/V.s)	I_{ON}/I_{OFF}	SS (mV/dec)	V_{th} (V)	Ref. No.
MoS_2	SiO_2	Back	-	1.9×10^6	59.51	-	[88]
	Al_2O_3	Top	-	5.0×10^6	64.84	-	
	HfO_2		-	1.7×10^7	60.64	-	
	TiO2		-	2.7×10^7	60.16	-	
WS2	SiO_2	Back	-	2.2×10^6	58.91	-	
	Al_2O_3	Top	-	5.2×10^6	59.31	-	
	HfO_2		-	1.5×10^7	60.53	-	
	TiO_2		-	2.5×10^7	60.12	-	
MoS2	SiO_2	Back	1.71	$\sim 10^3$	5.16		[93]
	Al_2O_3	Top	0.31	$\sim 10^5$	1.61		
MoS_2	Al_2O_3	Back	~33	$\sim 10^6$	~69	-	[95]
		Top	~145				
	SiO_2	Back	~11		~154	-	
		Top	~38				
WS_2	HfO_2	Back	-	-	>100	0.174	[96]
		Dual			< 75		
WS_2	SiO_2	Back	80	-	10^7	-48	[106]
	h-BN	Back	163			-58	
	h-BN	Dual	183				
MoS_2	SiO_2	Back	-	-	80	-	[107]
	HfO_2	Top			300		
	SiO_2 and HfO_2	Dual			200		
MoS_2	HfO_2	Dual	100	$\sim 10^6$	200	-3.7	[108]
	Al_2O_3				60		
	and Al_2O_3 /HfO_2						
MoS_2	SiO_2	Back	0.66	$\sim 10^3$	283	-	[109]
	Al_2O_3	Top	~22	$\sim 10^5$	255		
WS_2	SiO_2	Back	1.44	-	-	-	[110]
	h-BN	Top	115				

Numerous studies indicate that thin-film configurations of WS_2 nanosheets offer significant advantages over conventional FETs, demonstrating improved electrical transport properties. The performance of WS_2-FET devices is influenced by factors such as thickness of the nanosheet, layer count and surface area, all of which contribute to differences in device characteristics. Efforts to enhance WS_2-FET performance have been explored such as applying passivation layers, engineering metal contacts, and doping the surface with appropriate dopant atoms. These adjustments significantly influence key parameters including mobility, V_{th}, SS, Transconductance (g_m), and the I_{ON}/I_{OFF} current ratio. The study subsequently focused on junction modulation at the metal-semiconductor interface through contact engineering and examined the influence of surface doping on WS_2 nanosheets, which are crucial for improving the performance of FETs.

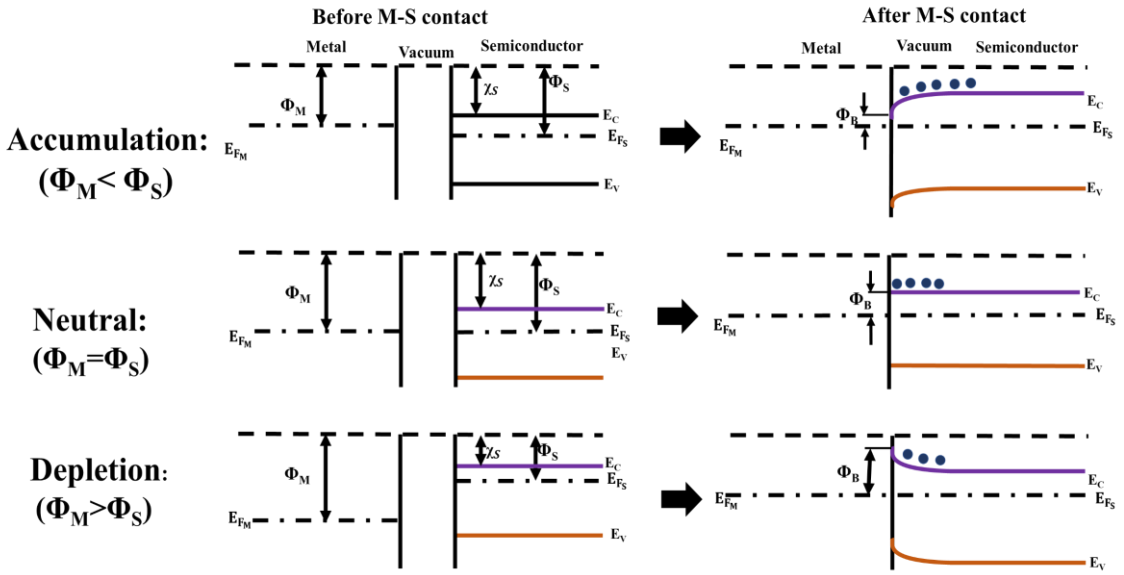

Fig. 2.6: The energy band diagram illustrates the Metal-Semiconductor interface for an n-type semiconductor: before and after contact, and the M-S junction can operate in three distinct modes: accumulation, neutral, and depletion

2.4. Metal-Semiconductor Interface:

The Metal-Semiconductor interface is a critical factor significantly affecting the performance of semiconductor devices. In transistors, Metal-semiconductor interfaces can exhibit two types of contacts: ohmic and non-ohmic, which correspond to linear and non-linear I-V characteristics, respectively [111]. Ohmic contacts are ideal for source and drain connections because they have low R_C and SBH, allowing for easier electron flow

and enhancing device performance [112]. In silicon-based MOSFETs, ohmic contacts are formed by heavy doping in the region beneath the contact metal through ion implantation, increasing the tunneling current [113]. As a result, the voltage drop across the contact is minimal compared to the voltage drop across the channel regions. Poor interface quality at M-S junctions can lead to non-ohmic contacts, which may dominate the conductivity and mobility due to the presence of high R_C and SBH.

Non-ohmic contacts are often explained using the Schottky-Mott theory, which links their behaviour to an interfacial layer at the M-S junction [113] In such contacts, the work function (Φ) is the energy difference between the Vacuum Level (E_{VAC}) and the Fermi level (E_F), with the semiconductor and metal work functions represented by Φ_S and Φ_M, respectively. The electron affinity of the semiconductor (χ_s) is the energy difference between E_{VAC} and the bottom of the conduction band E_C. The energy band diagram of an M-S junction highlights three types of energy barriers (Φ_B): accumulation ($\Phi_S < \Phi_M$), neutral ($\Phi_S = \Phi_M$), and depletion ($\Phi_S > \Phi_M$) as depicted in Fig. 2.6 [114]. When the semiconductor's work function is lower than that of the metal ($\Phi_S < \Phi_M$), the SBH is reduced, facilitating electron transport and creating an ohmic contact. In contrast, when $\Phi_S > \Phi_M$, electron passage is restricted, leading to a larger depletion region, increased SBH, and higher R_C. In the case of 2D materials, researchers have developed strategies to lower R_C and SBH, such as carrier injection, doping to alter the atomic structure of WS_2, using metals with lower work functions, and employing passivation layers to boost the performance of FET.

2.4.1. Doping of 2H-WS_2:

Doping in 2D materials is an essential method for adjusting their electronic band structure and improving functionality in electronic devices. In conventional semiconductors such as Si, doping is generally done using ion implantation or diffusion at elevated temperatures, which adds impurities (for example, phosphorus for n-type or boron for p-type) into the crystal lattice through substitutional doping [115–117]. Substitutional doping presents greater challenges because of the atomic thinness and distinctive surface properties of 2D materials. Instead, doping in 2D materials typically depends on different techniques, including surface doping, charge transfer doping, molecular doping, intercalation doping, chemical doping, etc. [118,119]. Doping in two-dimensional materials can greatly improve electronic characteristics like bandgap, carrier density, and conductivity, leading to direct uses in electronic devices. Enhancing doping

density can decrease contact resistance and the Schottky barrier height at the metal-semiconductor interface, crucial for effective charge injection and better device performance [120]. Numerous studies have demonstrated that doping techniques can effectively enhance the performance and reliability of devices based on 2D materials.

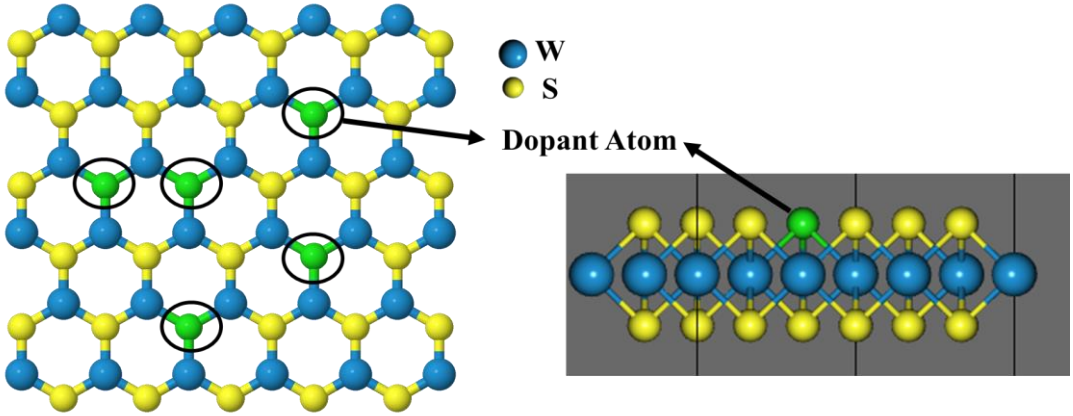

Fig. 2.7: Schematic representation of the atomic lattice structure of WS_2 with a dopant atom: (a) top view of the doped WS_2 lattice, and (b) side view of the doped WS_2, showing the dopant atom positioned on the top layer of WS_2

To modulate the electrical transport properties of TMDs, various doping methods have been proposed to achieve p-type or n-type conduction by introducing suitable dopant atoms. While many previous reports have shown improvements in either R_C, SBH, μ_{FE} etc., through various dopants such as LiF, hydrazine, Cu, or Rh-based organometallics. In TMDs like WS_2, the doping approach can be tailored based on the targeted atomic sites are Transition metal-site (W) or chalcogen-site (S) in the case of WS_2. According to Li et al., doping at the S-site, rather than the W-site, improves the material stability [118]. The dopant in the S-site is pictorially depicted in Fig. 2.7. Ghaffar et al. recently showed that substitutional doping at TMD interfaces can achieve Fermi level depinning, improve adhesion strength, and reduce the tunneling barrier, representing a significant improvement over conventional doping methods [119]. This approach offers a promising solution for inducing p-type contact polarity and reducing contact resistance in TMDs, paving the way for optimized TMD-based electronic devices. The modulation of the top S-vacancy site by the chemical dopant atom of $N^+/N_2^+ +$ resulted in a tenfold higher doping concentration and a fourfold increase in the Coulomb scattering coefficient demonstrated by Kim et al. [121]. This effect is attributed to the formation of shallow doping levels within the bandgap caused by S-vacancies, which makes them chemically active. The tunable p-type doping and favourable FET characteristics, such as low contact resistivity

of (8 ± 1)x102 Ω.cm were achieved after grown Nb doping in WS_2 films which promising for 2D-TMD transistors [122]. Siao. et. al reported that the dopant atom is simultaneously introduced into the lattice when WS_2 is growing through CVD technique [123]. Introducing a non-metallic dopant atom like Tin-oxide, Cl, etc. at the S-site in 2D materials can improve the metal-semiconductor interface, enhancing carrier concentration at the material's surface [124, 125]. This doping approach can lower the energy barrier, facilitating better charge transport and increasing tunnelling current, which is valuable for optimizing device performance in electronic applications. The n-type molecular doping process in WS_2 introduces additional electrons from dopant species into the semiconductor, significantly boosting carrier density based on factors like doping duration and dopant concentration in solution. A negative threshold voltage shift in Pentamethylrhodocene Dimer $(RhCpCp*)_2$-treated WS_2 FETs, observed after just 1 minute of treatment, highlights strong n-doping effects, as reported by Zhang et al. [126]. This results in an enhanced channel current, improved device field-effect mobility, and a higher current on/off ratio. However, Prolonged treatment durations result in the deterioration of doping efficiency in WS_2. A summary of various dopant atoms in TMD-FETs and their electrical properties is presented in Table 2.4. The reported work demonstrates a simultaneous and significant enhancement in all the electrical key parameters using a straightforward chlorine doping approach. Additionally, this work systematically compares the effect of doping on two different metal contacts (Cr and Ti) and demonstrates that the combined effect of work-function engineering and Cl doping leads to tunable and enhanced performance.

Table 2.4: Summary of Electrical Performance Parameters of TMD-Based FETs Enhanced via Substitutional Atomic Doping

TMD	Dopant atom	Dopant type	μ_{FE} ($cm^2/V.s$)		V_{th} (V)		n_s (cm^{-2})		I_{ON}/I_{OFF}		R_C (kΩ.μm)		SBH (meV)		Ref. No.
			Undoped	Doped	Undoped	Doped	Undoped	Doped	Undoped	Doped	Undoped	Doped	Undoped	Doped	
WS_2	Nitrogen	p	-	1.70	-	−12		1.10×10^{11}	-		-		-	-	[120]
WS_2	$(RhCpCp*)_2$	n	~2.2	4.25	0	-50		6×10^{12}	10^5	10^6	1140	7	112	57	[126]
MoS_2	Sm	p	3.08	4.35	-	-		-	5 x 10^3	3 x 10^4	-	-	-	-	[127]
MoS_2	P_2O_5	p	29.7	0.023	-	-	6.47 x 10^{11}	1.01x 10^{11}	10^3	10^3	-	-	-	-	[128]
WS_2	KI	n	5.8	30	28	-71	-	-	~10^6	~10^7	36.15	3.75	-	-	[129]
WS_2	V	p	0.11	0.24	-	-		-	10^6	10^5	-	-	-	-	[130]
MoS_2	BV	n	157.0	233.86	-	-	4.07 x 10^9	5.78 x10^6	-	-	-	-	-	-	[131]
MoS_2	PEI	n	20.4	32.7	-	-	-	-	~10^5	~10^2	0.00506	0.00457	-	-	[132]
WS_2	Na	p	10.23	15.61	-	-	-	-	10^5	10^4	_		-	-	[133]
WS_2	LiF	n	13.2	34.7	-	-	-	-	1.05×10^6	-	1.86	0.9	-	-	[134]
WS_2	TEA	n	9.8	28.6	-	-	8.8× 10^{11}	4.0 ×10^{12}	8.6 ×10^8	-	-	-	-	-	[135]
WS_2	PPh_3	n	14.1	74.6	-	-	1.0 x10^{12}	4.2x10^{11}	10^6	-	-	-	-	-	[136]
WS_2	$AuCl_3$	p		39.5					10^6						
WS_2	UV/ozone treatment	p	59.7	11.1	-	-	-	-	10^6	-	-	-	-	-	[137]
WS_2	Li^+	n	0.076	4.246	-	-	-	-	~10^3	~10^4	-	-	-	-	[138]
WS_2	S	n	-	-	-	-	-	-	_		0.059		46	20	[139]
WS_2	Cu	n	2.1	10.1	-	-	-	-	1.6x10^6	2.5x10^6	2200000	7400	123	89	[140]
MoS_2	Fe	n	~6	~54	-	-	~2.4 x 10^{11}	~2.4 x 10^{12}	~10^7	~10^8	117	0.67	-		[141]
MoS_2	NMP	n	-	-	-	-	6 x 10^{10}	2 x 10^{12}	-	-	-	-	-	-	[142]
MoS_2	KI	n	-	>70	-	-	-	1 x 10^{12}	~10^5	10^6	2.6	0.75	-	-	[143]
WS_2	Hydrazine	n	25	78	-	-	-	-	~10^5	~10^8	220	60	-	-	[144]

2.5. Methodologies/Approaches Applied:

In this research, the focus is on the preparation of WS_2 nanosheets for the fabrication of FET devices and the optimization of the parameters for the fabricated WS_2-FET devices. The research objectives were completed in the following phases:

- **WS_2 Nanosheet Synthesis and Spectroscopic Characterization:** Bulk WS_2 nanosheets were exfoliated using a low-cost, eco-friendly liquid-phase exfoliation process to reduce the nanosheet thickness from bulk WS_2 nanosheets. The exfoliated nanosheets were optimized using various spectroscopic instruments to identify material properties.
- **Optimizing the Doping Process on WS_2 Nanosheets:** For doping optimization on the WS_2 nanosheets, a straightforward doping method was employed. An n-type dopant material was used for the WS_2 nanosheets, achieved through a simple absorption process on the nanosheet surface.
- **Measurement of the IV Characteristics of Doped WS_2 Nanosheets:** The conductivity of doped and undoped WS_2 nanosheets was optimized by measuring the I-V characteristics.
- **Process Optimization for Fabrication of WS_2-based FETs:** For fabricating the FET, the laser writing lithography process was used to pattern the contact area and define the channel length and width. The fabrication process flow and metal deposition for the source-drain contact pads were also optimized.
- **I-V Measurement of the Fabricated WS_2-FET:** The electrical parameters of the final fabricated WS_2 FET device were characterized by measuring the I-V characteristics using Keithley 4200 SCS parameter analyzer in a probe station.

Bibliography:

[1] Roy, S. & Bermel, P. Electronic and optical properties of ultra-thin 2D tungsten disulfide for photovoltaic applications. Sol. Energy Mater. Sol. Cells., 174:370-379, 2018.

[2] Park, J., et al. Synthesis of uniform single layer WS_2 for tunable photoluminescence. Sci. Rep., 7(1):16121, 2017.

[3] Li, W., et al. Bandgap engineering of different stacking WS_2 bilayer under an external electric field. Solid State Commun., 225: 32-37, 2016.

[4] Romanov, R.I., et al. Thickness-Dependent Structural and Electrical Properties of WS_2 Nanosheets Obtained via the ALD-Grown WO_3 Sulfurization Technique as a Channel Material for Field-Effect Transistors. ACS Omega, 6:34429-34437, 2021.

[5] Abbas, O.A., et al. Solution-Based Synthesis of Few-Layer WS_2 Large Area Continuous Films for Electronic Applications. Sci. Rep., 10(1):1696, 2020.

[6] You, Y.G., et al. Atomic layer deposited Al_2O_3 passivation layer for few-layer WS_2 field effect transistors. Nanotechnology, 32(50): 505702, 2021.

[7] Ovchinnikov, D., et al. Electrical Transport Properties of Single-Layer WS_2. ACS Nano, 8(8): 8174-8181, 2014.

[8] Zhang, W., et al. Two-dimensional semiconductors with possible high room temperature mobility. Nano Res., 7(12): 1731-1737, 2014.

[9] Chen, T.-Y., et al. Comparative study on MoS_2 and WS_2 for electrocatalytic water splitting. Int. J. Hydrog. Energy, 38(28): 12302-12309, 2013.

[10] Quereda, J., et al. Scalable and low-cost fabrication of flexible WS_2 photodetectors on polycarbonate. Npj Flex. Electron, 6(1): 23, 2022.

[11] Carey, T., et al. High-Mobility Flexible Transistors with Low-Temperature Solution-Processed Tungsten Dichalcogenides. ACS Nano, 17(3): 2912-2922, 2023.

[12] Magnozzi, M., et al. Local Optical Properties in CVD-Grown Monolayer WS_2 Flakes. J. Phys. Chem. C., 125(29): 16059-16065, 2021.

[13] Balasubramanyam, S., et al. Edge-Site Nanoengineering of WS_2 by Low-Temperature Plasma-Enhanced Atomic Layer Deposition for Electrocatalytic Hydrogen Evolution. Chem. Mater., 31(14): 5104-5115, 2019.

[14] Liu, L., Kumar, et al. Performance Limits of Monolayer Transition Metal Dichalcogenide Transistors. IEEE Trans. Electron Devices, 58(9): 3042-3047, 2011.

[15] Jin, Z., Li, X., et al. Intrinsic transport properties of electrons and holes in monolayer transition-metal dichalcogenides. Phys. Rev. B., 90(4): 045422, 2014.

[16] Liu, X., et al. High Performance Field-Effect Transistor Based on Multilayer Tungsten Disulfide. ACS Nano, 8(10): 10396-10402, 2014.

[17] Zhu, Z.Y., et al. Giant spin-orbit-induced spin splitting in two-dimensional transition-metal dichalcogenide semiconductors. Phys. Rev. B., 84(15): 153402, 2011.

[18] Gong, Y., et al. High flex cycle testing of CVD monolayer WS_2 TFTs on thin flexible polyimide. 2D Mater., 3(2): 021008, 2016.

[19] Brent, J.R., et al. Synthetic approaches to two-dimensional transition metal dichalcogenide nanosheets. Prog. Mater. Sci., 89: 411-478, 2017.

[20] Kuc, A. & Heine, T. The electronic structure calculations of two-dimensional transition-metal dichalcogenides in the presence of external electric and magnetic fields. Chem. Soc. Rev., 44(9): 2603-2614, 2015.

[21] Saha, D. & Kruse, P. Editors' Choice-Review-Conductive Forms of MoS_2 and Their Applications in Energy Storage and Conversion. J. Electrochem. Soc., 167(12): 126517, 2020.

[22] He, Q., et al. Vertically Aligned Ultrathin 1T-WS_2 Nanosheets Enhanced the Electrocatalytic Hydrogen Evolution. Nanoscale Res. Lett., 13(1): 167, 2018.

[23] Paudel, D.R., et al. Interface modulation induced by the 1T Co-WS_2 shell nanosheet layer at the metallic $NiTe_2$/Ni core-nanoskeleton: Glib electrode-kinetics for HER, OER, and ORR. Nano Energy, 102:107712, 2022.

[24] Meng, C., et al. Recent Modification Strategies of MoS_2 for Enhanced Electrocatalytic Hydrogen Evolution. Molecules, 25(5): 1136, 2020.

[25] Toh, R.J., et al. 3R phase of MoS_2 and WS_2 outperforms the corresponding 2H phase for hydrogen evolution. Chem. Commun., 53(21): 3054-3057, 2017.

[26] Wang, Q.H., et al. Electronics and optoelectronics of two-dimensional transition metal dichalcogenides. Nat. Nanotechnol, 7(11):699-712, 2012.

[27] Falahati, K., et al. Band tuning in WS_2 monolayer via substitutional doping. Micro Nanostructures, 164: 107120, 2022.

[28] Xu, D., et al. High Yield Exfoliation of WS_2 Crystals into 1-2 Layer Semiconducting Nanosheets and Efficient Photocatalytic Hydrogen Evolution from WS_2 /CdS Nanorod Composites. ACS Appl. Mater. Interfaces, 10(3): 2810-2818, 2018.

[29] Wan, Y., et al. Low-defect-density WS_2 by hydroxide vapor phase deposition. Nat. Commun., 13(1): 4149, 2022.

[30] Voiry, D., et al. Enhanced catalytic activity in strained chemically exfoliated WS_2 nanosheets for hydrogen evolution. Nat. Mater., 12(9): 850-855, 2013.

[31] Friedman, A.L., et al. Evidence for Chemical Vapor Induced 2H to 1T Phase Transition in MoX2 (X = Se, S) Transition Metal Dichalcogenide Films. Sci. Rep., 7(1): 3836, 2017.

[32] Kumar, P., et al. Phase engineering of seamless heterophase homojunctions with co-existing 3R and 2H phases in WS_2 monolayers. Nanoscale., 10(7): 3320-3330, 2018.

[33] Jung, Y., et al. WOx-driven growth of 2H- and 3R-WS_2 multilayers by physical vapor deposition. Appl. Surf. Sci., 682: 161676, 2025.

[34] Yang, R., et al. Effect of layer and stacking sequence in simultaneously grown 2H and 3R WS_2 atomic layers. Nanotechnology, 30(34): 345203, 2019.

[35] Opoku, F., et al. Role of MoS_2 and WS_2 monolayers on photocatalytic hydrogen production and the pollutant degradation of monoclinic $BiVO_4$: a first-principles study. New J. Chem., 41(20): 11701-11713, 2017.

[36] Gavhane, D.S., et al. Selective Vertical and Horizontal Growth of 2D WS_2 Revealed by In Situ Thermolysis using Transmission Electron Microscopy. Adv. Funct. Mater., 32(1): 2106450, 2022.

[37] Pimenta, M.A., et al. Comparative Study of Raman Spectroscopy in Graphene and MoS_2 -type Transition Metal Dichalcogenides. Acc. Chem. Res., 48(1): 41-47, 2015.

[38] He, X., et al. Strain engineering in monolayer WS_2, MoS_2, and the WS_2/MoS_2 heterostructure. Appl. Phys. Lett., 109(17): 173105, 2016.

[39] Li, Z., et al. Chemical passivation of 2D transition metal dichalcogenides: strategies, mechanisms, and prospects for optoelectronic applications. Nanoscale, 16(20): 9728-9741, 2024.

[40] Dutta, T., et al. Electronic properties of 2D materials and their junctions. Nano Mater. Sci., 6(1): 1-23, 2024.

[41] Terrones, H., et al. Novel hetero-layered materials with tunable direct band gaps by sandwiching different metal disulfides and diselenides. Sci. Rep., 3(1): 1549, 2013.

[42] Muoi, D., et al. Electronic properties of WS_2 and WSe_2 monolayers with biaxial strain: A first-principles study. Chem. Phys., 519: 69-73, 2019.

[43] Muoi, D., et al. Low-energy bands and optical properties of monolayer WS_2. Optik., 209: 164581, 2020.

[44] Yang, K., et al. Tuning electronic behaviors of WS_2 by molecular doping. Mater. Today Commun., 33: 104226, 2022.

[45] Poornimadevi, C., et al. Tuning the electronic properties of WS_2 monolayer by doping transition metals: DFT Approach. Mater. Sci. Semicond. Process., 157: 107339, 2023.

[46] Kang, K., et al. The effects of substitutional Fe-doping on magnetism in MoS_2 and WS_2 monolayers. Nanotechnology, 32(9): 095708, 2021.

[47] Zhu, Y.-Y. & Zhang, J.-M. The structural, magnetic and electronic properties of p-type and n-type doped monolayer WS_2 systems. Superlattices Microstruct., 112: 619-627, 2017.

[48] Chanana, A. & Mahapatra, S. Density functional theory based study of chlorine doped WS_2-metal interface. Appl. Phys. Lett., 108(10): 103107, 2016.

[49] Zhang, F., et al. Carbon doping of WS_2 monolayers: Bandgap reduction and p-type doping transport. Sci. Adv., 5(5): eaav5003, 2019.

[50] Tran, P.D., et al. Water electrolysis and photoelectrolysis on electrodes engineered using biological and bio-inspired molecular systems. Energy Environ. Sci., 3(6):727, 2010.

[51] Batmunkh, M., et al. Phosphorene and Phosphorene-Based Materials - Prospects for Future Applications. Adv. Mater., 28(39): 8586-8617, 2016.

[52] Liu, H.-L., et al. Optical properties of monolayer transition metal dichalcogenides probed by spectroscopic ellipsometry. Appl. Phys. Lett., 105(20): 201905, 2014.

[53] Song, H., et al. Modification of WS_2 nanosheets with controllable layers via oxygen ion irradiation. Appl. Surf. Sci., 439: 240-245, 2018.

[54] Li, Y., et al. Accurate identification of layer number for few-layer WS_2 and WSe_2 via spectroscopic study. Nanotechnology, 29(12): 124001, 2018.

[55] Shi, Y., et al. van der Waals Epitaxy of MoS_2 Layers Using Graphene As Growth Templates. Nano Lett., 12(6): 2784-2791, 2012.

[56] Huang, H., et al. Water-Soluble Monolayer Molybdenum Disulfide Quantum Dots with Upconversion Fluorescence. Part. Part. Syst. Charact., 32(1): 72-79, 2015.

[57] Tong, X., et al. Advances in MoS_2-Based Field Effect Transistors (FETs). Nano-Micro Lett., 7(3): 203-218 (2015.

[58] Chaves, A., et al. Bandgap engineering of two-dimensional semiconductor materials. Npj 2D Mater. Appl., 4(1): 29, 2020.

[59] Beal, A.R. & Hughes, H.P. Kramers-Kronig analysis of the reflectivity spectra of 2H-MoS_2, 2H-$MoSe_2$ and 2H-$MoTe_2$. J. Phys. C Solid State Phys., 12(5): 881-890, 1979.

[60] Ruppert, C., et al. Optical Properties and Band Gap of Single- and Few-Layer $MoTe_2$ Crystals. Nano Lett., 14(11): 6231-6236, 2014.

[61] Islam, M.R., et al. Impact of strain on the electronic, phonon, and optical properties of monolayer transition metal dichalcogenides XTe_2 (X = Mo and W). Phys. Scr., 97(4): 045806, 2022.

[62] Novoselov, K.S., et al. Electric Field Effect in Atomically Thin Carbon Films. Science, 306(5696):666–669, 2004.

[63] Divigalpitiya, W.M.R., et al. Inclusion Systems of Organic Molecules in Restacked Single-Layer Molybdenum Disulfide. Science., 246(4928): 369-371, 1989.

[64] Coleman, J.N., et al. Two-Dimensional Nanosheets Produced by Liquid Exfoliation of Layered Materials. Science., 331(6017): 568-571, 2011.

[65] Liu, J., et al. A comprehensive comparison study on the vibrational and optical properties of CVD-grown and mechanically exfoliated few-layered WS_2. J. Mater. Chem. C., 5(43): 11239-11245, 2017.

[66] Radisavljevic, B., et al. Single-layer MoS_2 transistors. Nat. Nanotechnol., 6(3): 147-150, 2011.

[67] Falin, A., et al. Mechanical Properties of Atomically Thin Tungsten Dichalcogenides: WS_2, WSe_2, and WTe_2. ACS Nano, 15(2): 2600-2610, 2021.

[68] Mei, L., et al. Phase-switchable preparation of solution-processable WS_2 mono- or bilayers. Nat. Synth., 2024. https://www.nature.com/articles/s44160-024-00679-2

[69] D'Olimpio, G., et al. Dimethyl 2-Methylglutarate (Iris): A Green Platform for Efficient Liquid-Phase Exfoliation of 2D Materials. Adv. Sustain. Syst., 6(11): 2200277, 2022.

[70] Tham, H.M., et al. WS_2 deposition on cross-linked polyacrylonitrile with synergistic transformation to yield organic solvent nanofiltration membranes. J. Membr. Sci., 588: 117219, 2019.

[71] Jha, R. & Guha, P.K. An effective liquid-phase exfoliation approach to fabricate tungsten disulfide into ultrathin two-dimensional semiconducting nanosheets. J. Mater. Sci., 52: 7256-7268, 2017.

[72] An, G.H., et al. Growth mode control of CVD-grown WS_2 monolayer flakes via O_2 pre-annealing for organic surfactant oxidation. Appl. Surf. Sci., 585: 152564, 2022.

[73] Xu, M., et al. CVD Synthesis of Twisted Bilayer WS_2 with Tunable Second Harmonic Generation. Adv. Mater., 36(19): 2313638, 2024.

[74] Yan, J., et al. CVD controlled preparation and growth mechanism of 2H-WS_2 nanosheets. Vacuum., 207: 111564, 2023.

[75] Meng, D., et al. Hierarchical WS_2-WO_3 Nanohybrids with Flower-like p-n Heterostructures for Trimethylamine Detection. Nanomaterials., 14(16): 1322, 2024.

[76] Santhosh, et al. A novel, facile, and efficient two-step hydrothermal route for WS_2 nanosheets and its optimistic exposure as competent industrial-level sonocatalyst. J. Mater. Sci. Mater. Electron., 32(7): 9357-9367, 2021.

[77] Govindasamy, M., et al. Synergetic effect of the ultrasonic-assisted hydrothermal process on the photocatalytic performance of MoS_2 and WS_2 nanoparticles. J. Mater. Sci. Mater. Electron., 33(11): 8858-8867, 2022.

[78] Altuntepe, A., et al. Large-scale synthesis of homogeneous WS_2 films by physical vapor deposition. Eurasian J. Sci. Eng. Technol., 4(1): 36-41, 2023.

[79] Lim, Y.R., et al. Roll-to-Roll Production of Layer-Controlled Molybdenum Disulfide: A Platform for 2D Semiconductor-Based Industrial Applications. Adv. Mater., 30(5): 1705270, 2018.

[80] Wang, X., et al. Location-specific growth and transfer of arrayed MoS_2 monolayers with controllable size. 2D Mater., 4(2): 025093, 2017.

[81] Mupparapu, R., et al. Integration of two-dimensional transition metal dichalcogenides with Mie-resonant dielectric nanostructures. Adv. Phys. X., 5(1): 1734083, 2020.

[82] Wang, Y., et al. Electrochemical Delamination of CVD-Grown Graphene Film: Toward the Recyclable Use of Copper Catalyst. ACS Nano, 5(12): 9927-9933, 2011.

[83] Van Ngoc, H., et al. PMMA-Etching-Free Transfer of Wafer-scale Chemical Vapor Deposition Two-dimensional Atomic Crystal by a Water Soluble Polyvinyl Alcohol Polymer Method. Sci. Rep., 6(1): 33096, 2016.

[84] Cun, H., et al. Centimeter-Sized Single-Orientation Monolayer Hexagonal Boron Nitride With or Without Nanovoids. Nano Lett., 18(2): 1205-1212, 2018.

[85] Yang, R., et al. Multilayer MoS_2 transistors enabled by a facile dry-transfer technique and thermal annealing. J. Vac. Sci. Technol. B Nanotechnol. Microelectron. Mater. Process. Meas. Phenom., 32(6): 061203, 2014.

[86] Li, M.-Y., et al. Wafer-Scale Bi-Assisted Semi-Auto Dry Transfer and Fabrication of High-Performance Monolayer CVD WS_2 Transistor. In: 2022 IEEE Symposium on VLSI Technology and Circuits (VLSI Technology and Circuits). pp. 290-291. IEEE, Honolulu, HI, USA (2022)

[87] Yoon, M. A., et al. Surface Properties of CVD-Grown Graphene Transferred by Wet and Dry Transfer Processes. Sensors, 22(10): 3944, 2022.

[88] Prasanna Kumar, S., et al. Changes in transconductance(gm) and Ion/Ioff with high-K dielectrics in MX_2 monolayer 10 nm channel double gate n-MOSFET. Superlattices Microstruct, 111: 642-648, 2017.

[89] Mounir, A., et al. Compact I-V model for back-gated and double-gated TMD FETs. Solid-State Electron, 207: 108702, 2023.

[90] Acar, M., et al. Single-step, large-area, variable thickness sputtered WS_2 film-based field effect transistors. Ceram. Int., 46(17): 26854-26860, 2020.

[91] Yang, E., et al. Realization of Extremely High-Gain and Low-Power in nMOS Inverter Based on Monolayer WS_2 Transistor Operating in Subthreshold Regime. ACS Nano, 18(34): 22965-22977, 2024.

[92] Cui, Y., et al. High-Performance Monolayer WS_2 Field-Effect Transistors on High-κ Dielectrics. Adv. Mater., 27(35): 5230-5234, 2015.

[93] Chen, T., et al. Homogeneous dual-gate MoS_2 field-effect transistors integrated by atomic layer deposition-based film synthesis. J. Mater. Sci. Mater. Electron., 31(7): 5485-5491, 2020.

[94] Lin, Y.-S., et al. Low-Temperature Physical Adsorption for the Nucleation of Sub-10 nm Al_2O_3 Gate Stack on Top-Gated WS_2 Transistors. ACS Appl. Electron. Mater., 2(5): 1289-1294, 2020.

[95] Bolshakov, P., et al. Improvement in top-gate MoS_2 transistor performance due to high quality backside Al_2O_3 layer. Appl. Phys. Lett., 111(3): 032110, 2017.

[96] Pang, C.-S., et al. Thickness-Dependent Study of High- Performance WS_2-FETs With Ultrascaled Channel Lengths. IEEE Trans. Electron Devices, 68(4): 2123-2129, 2021.

[97] Cheng, L., et al. Atomic Layer Deposition of a High- *k* Dielectric on MoS_2 Using Trimethylaluminum and Ozone. ACS Appl. Mater. Interfaces., 6(15): 11834-11838, 2014.

[98] Yang, J., et al. Improved Growth Behavior of Atomic-Layer-Deposited High- *k* Dielectrics on Multilayer MoS_2 by Oxygen Plasma Pretreatment. ACS Appl. Mater. Interfaces., 5(11): 4739-4744, 2013.

[99] Kim, S.K., et al. Low Temperature (<100 °C) Deposition of Aluminum Oxide Thin Films by ALD with O[sub 3] as Oxidant. J. Electrochem. Soc., 153(5): F69, 2006.

[100] Gao, Q., et al. Effect of Back-Gate Voltage on the High-Frequency Performance of Dual-Gate MoS_2 Transistors. Nanomaterials, 11(6): 1594, 2021.

[101] Zhan, L., et al. Electrical Properties of Dual-Gate, Ultrashort Monolayer WS_2 Transistors. IEEE Electron Device Lett., 1-1, 2024.

[102] Jin, L. & Koester, S.J. Contact Gating in Dual-Gated WS_2 MOSFETs With Semi-Metallic Bi Contacts. IEEE Electron Device Lett., 43(9):1575-1578, 2022.

[103] Jin, L., et al. High-Performance WS_2 MOSFETs with Bilayer WS_2 Contacts. ACS Omega, 9(29): 32159-32166, 2024.

[104] Illarionov, Y.Yu., et al. Insulators for 2D nanoelectronics: the gap to bridge. Nat. Commun., 11(1): 3385, 2020.

[105] Li, S.-L., et al. Charge transport and mobility engineering in two-dimensional transition metal chalcogenide semiconductors. Chem. Soc. Rev., 45(1): 118-151, 2016.

[106] Iqbal, M.W., et al. High-mobility and air-stable single-layer WS_2 field-effect transistors sandwiched between chemical vapor deposition-grown hexagonal BN films. Sci. Rep., 5(1): 10699, 2015.

[107] Patoary, N.H., et al. Analysis and EOT Scaling on Top- and Double-Gate 2D CVD-Grown Monolayer MoS_2 FETs. Adv. Electron. Mater., 10(11): 2400152, 2024.

[108] Bolshakov, P., et al. Dual-gate MoS_2 transistors with sub-10 nm top-gate high-k dielectrics. Appl. Phys. Lett., 112(25): 253502, 2018.

[109] Kim, H., et al. Optimized single-layer MoS_2 field-effect transistors by non-covalent functionalisation. Nanoscale, 10(37): 17557-17566, 2018.

[110] Phan, N.A.N., et al. Enhanced Performance of WS_2 Field-Effect Transistor through Mono and Bilayer h-BN Tunneling Contacts. Small, 18(13): 2105753, 2022.

[111] Li, S.S. Metal-Semiconductor Contacts. In: Li, S.S. (ed.) Semiconductor Physical Electronics. pp. 284-333. Springer New York, New York, NY, 2006.

[112] Lizzit, D., et al. Ohmic Behavior in Metal Contacts to n/p-Type Transition-Metal Dichalcogenides: Schottky versus Tunneling Barrier Trade-off. ACS Appl. Nano Mater., 6(7): 5737-5746, 2023.

[113] Kao, K.C. Charge Carrier Injection from Electrical Contacts. In: Dielectric Phenomena in Solids. Elsevier, pp. 327-380, 2004.

[114] Tong, Y., et al. A metal/semiconductor contact induced Mott-Schottky junction for enhancing the electrocatalytic activity of water-splitting catalysts. Sustain. Energy Fuels., 7(1): 12-30, 2023.

[115] Sproul, A.B. & Green, M.A. Improved value for the silicon intrinsic carrier concentration from 275 to 375 K. J. Appl. Phys., 70(2): 846-854, 1991.

[116] Acceptor atom. (n.d.) McGraw-Hill Concise Encyclopedia of Physics. (2002). Retrieved November 27, 2024. https://encyclopedia2.thefreedictionary.com/acceptor+atom.

[117] Fundamentals: Doping: n- and p-semiconductors. www.halbleiter.org. Retrieved 2016-12-19.

[118] Li, H., et al. Nonmetal doping induced electronic and magnetic properties in $MoSe_2$ monolayer. Chem. Phys. Lett., 692: 69-74, 2018.

[119] Ghaffar, A., et al. Substitutional Doping Strategies for Fermi Level Depinning and Enhanced Interface Quality in WS_2 -Metal Contacts. ACS Appl. Electron. Mater., 6(6): 4587-4600, 2024.

[120] Tang, B., et al. Direct n- to p-Type Channel Conversion in Monolayer/Few-Layer WS_2 Field-Effect Transistors by Atomic Nitrogen Treatment. ACS Nano., 12(3): 2506-2513, 2018.

[121] Kim, K.S., et al. Atomic Layer Engineering of TMDs by Modulation of Top Chalcogen Atoms: For Electrical Contact and Chemical Doping. ACS Appl. Electron. Mater., 4(8): 3794-3800, 2022.

[122] Schulpen, J.J.P.M., et al. Nb Doping and Alloying of 2D WS_2 by Atomic Layer Deposition for 2D Transition Metal Dichalcogenide Transistors and HER Electrocatalysts. ACS Appl., Nano Mater., 7(7): 7395-7407, 2024.

[123] Siao, M., et al. Embedment of Multiple Transition Metal Impurities into WS_2 Monolayer for Bandstructure Modulation. Small, 17(17): 2007171, 2021.

[124] Esfandiari, M., et al. High-performance large-area WS_2-based transistors by a novel tin-oxide assisted liquid-phase exfoliation: doping adjustment by plasma treatment. 2D Mater., 8(2): 025013, 2021.

[125] Kim, K.H., et al. Effect of large work function modulation of MoS_2 by controllable chlorine doping using a remote plasma. J. Mater. Chem. C., 8(5): 1846-1851, 2020.

[126] Zhang, S., et al. Control of the Schottky barrier height in monolayer WS_2 FETs using molecular doping. AIP Adv., 12(8): 085222, 2022.

[127] Li, S., et al. Enhanced Electrical Performance of Monolayer MoS_2 with Rare Earth Element Sm Doping. Nanomaterials, 11(3): 769, 2021.

[128] Lee, J.S., et al. Characteristics of p-Type Conduction in P-Doped MoS_2 by Phosphorous Pentoxide during Chemical Vapor Deposition. Nanomaterials, 9(9): 1278, 2019.

[129] Iqbal, M.W., et al. Tailoring the electrical and photo-electrical properties of a WS_2 field effect transistor by selective n-type chemical doping. RSC Adv., 6(29): 24675-24682, 2016.

[130] Gao, B., et al. Electrical Polarity Modulation in V-Doped Monolayer WS_2 for Homogeneous CMOS Inverters. Small, 20(43): 2402217, 2024.

[131] Jang, J., et al. Reduced dopant-induced scattering in remote charge-transfer-doped MoS_2 field-effect transistors. Sci. Adv., 8(38): eabn3181, 2022.

[132] Du, Y., et al. Molecular Doping of Multilayer MoS_2 Field-Effect Transistors: Reduction in Sheet and Contact Resistances. IEEE Electron Device Lett., 34(10): 1328-1330, 2013.

[133] Xie, J., et al. Vapor-Liquid-Solid Growth of Morphology-Tailorable WS_2 toward P-Type Monolayer Field-Effect Transistors. ACS Appl. Mater. Interfaces., 14(40): 45716-45724, 2022.

[134] Khalil, H.M.W., et al. Highly Stable and Tunable Chemical Doping of Multilayer WS_2 Field Effect Transistor: Reduction in Contact Resistance. ACS Appl. Mater. Interfaces., 7(42): 23589-23596, 2015.

[135] Liang, J., et al. Reversible electron doping in monolayer WS_2 via a chemical strategy. 2D Mater., 6(2): 025003, 2019.

[136] Ma, X., et al. Efficient doping modulation of monolayer WS_2 for optoelectronic applications. Chin. Phys. B., 28(3): 037803, 2019.

[137] Bae, J., et al. Achieving Ambipolar Transport Characteristics in the n-WS_2 Channel via Remote p-Doping and its Enhancement-Mode Ambipolar Field-Effect Transistor Operation. ACS Appl. Electron. Mater., 6(10): 7416-7423, 2024.

[138] Wang, H., et al. An ambipolar transistor based on a monolayer WS_2 using lithium ions injection. Mater. Res. Express., 7(7): 076302, 2020.

[139] Ansh, et al. Chalcogen-Assisted Enhanced Atomic Orbital Interaction at TMD-Metal Interface and Sulfur Passivation for Overall Performance Boost of 2-D TMD FETs. IEEE Trans. Electron Devices., 67(2): 717-724, 2020.

[140] Liu, M., et al. Enhanced carrier transport by transition metal doping in WS_2 field effect transistors. Nanoscale., 12(33): 17253-17264, 2020.

[141] Li, H., et al. Reducing Contact Resistance and Boosting Device Performance of Monolayer MoS_2 by In Situ Fe Doping. Adv. Mater., 34(18): 2200885, 2022.

[142] Sunwoo, H. & Choi, W. Tunable, stable, and reversible n-type doping of MoS_2 via thermal treatment in N-methyl-2-pyrrolidone. Nanotechnology, 33(50): 50LT01, 2022.

[143] Hemanjaneyulu, K., et al. MoS_2 Doping Using Potassium Iodide for Reliable Contacts and Efficient FET Operation. IEEE Trans. Electron Devices., 66(7): 3224-3228, 2019.

[144] Chee, S.-S., et al. Sulfur vacancy-induced reversible doping of transition metal disulfides via hydrazine treatment. Nanoscale., 9(27): 9333-9339, 2017.